

Stratigraphy of the Caloris basin, Mercury: Implications for volcanic history and basin impact melt



Carolyn M. Ernst ^{a,*}, Brett W. Denevi ^a, Olivier S. Barnouin ^a, Christian Klimczak ^{b,c}, Nancy L. Chabot ^a, James W. Head ^d, Scott L. Murchie ^a, Gregory A. Neumann ^e, Louise M. Prockter ^a, Mark S. Robinson ^f, Sean C. Solomon ^{b,g}, Thomas R. Watters ^h

^a The Johns Hopkins University Applied Physics Laboratory, Laurel, MD 20723, USA

^b Department of Terrestrial Magnetism, Carnegie Institution of Washington, Washington, DC 20015, USA

^c Department of Geology, University of Georgia, Athens, GA 30602, USA

^d Department of Earth, Environmental and Planetary Sciences, Brown University, Providence, RI 02912, USA

^e Planetary Geodynamics Laboratory, NASA Goddard Space Flight Center, Greenbelt, MD 20771, USA

^f School of Earth and Space Exploration, Arizona State University, Tempe, AZ 85287, USA

^g Lamont-Doherty Earth Observatory, Columbia University, Palisades, NY 10964, USA

^h Center for Earth and Planetary Studies, National Air and Space Museum, Smithsonian Institution, Washington, DC 20560, USA

ARTICLE INFO

Article history:

Received 11 August 2014

Revised 25 October 2014

Accepted 1 November 2014

Available online 15 November 2014

Keywords:

Mercury

Mercury, surface

Cratering

Volcanism

Geological processes

ABSTRACT

Caloris basin, Mercury's youngest large impact basin, is filled by volcanic plains that are spectrally distinct from surrounding material. Post-plains impact craters of a variety of sizes populate the basin interior, and the spectra of the material they have excavated enable the thickness of the volcanic fill to be estimated and reveal the nature of the subsurface. The thickness of the interior volcanic plains is consistently at least 2.5 km, reaching 3.5 km in places, with thinner fill toward the edge of the basin. No systematic variations in fill thickness are observed with long-wavelength topography or azimuth. The lack of correlation between plains thickness and variations in elevation at large horizontal scales within the basin indicates that plains emplacement must have predated most, if not all, of the changes in long-wavelength topography that affected the basin. There are no embayed or unambiguously buried (ghost) craters with diameters greater than 10 km in the Caloris interior plains. The absence of such ghost craters indicates that one or more of the following scenarios must hold: the plains are sufficiently thick to have buried all evidence of craters that formed between the Caloris impact event and the emplacement of the plains; the plains were emplaced soon after basin formation; or the complex tectonic deformation of the basin interior has disguised wrinkle-ridge rings localized by buried craters. That low-reflectance material (LRM) was exposed by every impact that penetrated through the surface volcanic plains provides a means to explore near-surface stratigraphy. If all occurrences of LRM are derived from a single layer, the subsurface LRM deposit is at least 7.5–8.5 km thick and its top likely once made up the Caloris basin floor. The Caloris-forming impact would have generated a layer of impact melt 3–15 km thick; such a layer could account for the entire thickness of LRM. This material would have been derived from a combination of lower crust and upper mantle.

© 2014 Elsevier Inc. All rights reserved.

1. Introduction

Images of Mercury acquired by the Mariner 10 (e.g., Murray et al., 1974; Strom et al., 1975; Trask and Guest, 1975) and MErcury Surface, Space ENvironment, GEochemistry, and Ranging (MESSENGER) (e.g., Head et al., 2008; Murchie et al., 2008; Robinson et al., 2008) spacecraft revealed large areas of smooth

plains, characterized by level to gently sloping surfaces and a comparatively low density of superposed impact craters. Recent mapping from MESSENGER orbital data has demonstrated that nearly 30% of Mercury's surface is covered by such smooth plains (Denevi et al., 2013a), the largest expanse of which covers much of Mercury's northern high latitudes (Head et al., 2011). The higher-spatial-resolution MESSENGER data have provided confirmation that the majority of the smooth plains are of volcanic origin (Head et al., 2008, 2011; Murchie et al., 2008; Robinson et al., 2008; Denevi et al., 2009, 2013a).

* Corresponding author.

The widespread intercrater plains, characterized by locally level surfaces with a high density of small superposed impact craters (Trask and Guest, 1975), have similarly been proposed by many to be volcanic in origin, emplaced near the end of the late heavy bombardment of the inner Solar System and strongly textured by multiple impacts (e.g., Murray et al., 1975; Trask and Guest, 1975; Malin, 1976; Cintala et al., 1977; Strom, 1977; Denevi et al., 2009, 2013b; Whitten et al., 2014a). If such an interpretation for the origin of intercrater plains is correct, then most of Mercury's surface is volcanic and the product of multiple generations of resurfacing (e.g., Marchi et al., 2013). Stratigraphic analyses suggest that sequential volcanic deposits formed large portions of Mercury's upper crust, at least to a depth of 5 km (Denevi et al., 2009; Ernst et al., 2010; Head et al., 2011). The considerable vertical and horizontal extent of volcanic deposits in Mercury's upper crust suggests that volcanism played a more substantial role in the surface evolution of the innermost planet than in that of the Moon.

Among Mercury's largest expanses of smooth volcanic plains are those interior to the Caloris basin, 1525 km by 1315 km in diameter (Fassett et al., 2009) and centered at 31.5°N, 162.7°E. These plains, classified as high-reflectance red plains (HRP) (Murchie et al., 2008; Robinson et al., 2008; T.R. Watters et al., 2009b), are spectrally distinct from the Caloris rim structure and the smooth plains exterior to the basin. Post-plains impact craters of a variety of sizes in the basin interior have excavated material from depth and thus provide a means for exploring near-surface stratigraphy. Many of these craters excavated low-reflectance material (LRM) (Murchie et al., 2008; Robinson et al., 2008; Denevi et al., 2009), indicating the presence of a spectrally distinct unit beneath much if not all of the HRP material. Estimates of the fill thickness near the center of Caloris from MESSENGER flyby images ranged from 1 to 4 km, indicating the presence of a substantial volume, rather than only a thin veneer, of volcanic plains material on the surface (T.R. Watters et al., 2009b; Ernst et al., 2010). Although the flyby images provided full coverage of the Caloris interior, the resolution and viewing geometries available were insufficient to address several key questions: How many flooded craters are in the Caloris interior plains? How thick is the fill across the entire basin? How quickly were the plains emplaced?

The images acquired during MESSENGER's first two years of orbital operations provide a means to address these questions. We first constructed a high-resolution monochrome mosaic of the Caloris interior. Although the calibration of the color data presented considerable challenges (Keller et al., 2013), a color mosaic was then successfully produced. From these two data products, we classified craters according to their morphological and color properties. On the basis of these classifications, we here present determinations at multiple locations of the thickness of the high-reflectance plains inside Caloris basin and an assessment of the nature of the subsurface, following the techniques detailed by Ernst et al. (2010). From these thickness measurements, we derive estimates for the volume, timing, and duration of the flooding, and we discuss implications for the nature of Mercury's low-reflectance material in this region.

2. Methods

We used a combination of datasets acquired by the MESSENGER Mercury Dual Imaging System (MDIS) wide-angle camera (WAC) and narrow-angle camera (NAC) (Hawkins et al., 2007, 2009) to perform our analysis. To date, MDIS has acquired global color and high-resolution monochrome base maps of Mercury (at mean pixel scales of approximately 900 m and 170 m, respectively), as well as thousands of targeted color and monochrome observations

(pixel scales as good as 80 m in color and 10 m in monochrome in the northern hemisphere). These data, taken under illumination and observation geometries optimized for observing both color and morphology, allow detailed co-mapping of spectral and geologic features across Mercury's surface.

We focus here on the volcanically flooded interior of Caloris basin, illustrated in Fig. 1. With MDIS WAC and NAC images optimized for viewing surface morphology, we identified all craters of diameter greater than or equal to 10 km. The 10 km limit was chosen to eliminate most secondary craters, which dominate crater populations at smaller sizes on Mercury (Strom et al., 2008; Chapman et al., 2011). MDIS multispectral WAC images were used to examine the color properties of each crater's ejecta, rim, floor, and central peak structures to determine whether LRM was exposed by the impact from beneath the surface HRP. We applied principal component analysis to color image mosaics, and we constructed enhanced-color images (e.g., Fig. 1) with the second principal component (PC2), the first principal component (PC1), and the relative color (the ratio of the reflectance at 430 nm wavelength to that at 1000 nm) assigned to the red, green, and blue channels, respectively. Such a color projection is well suited to display LRM prominently (Fig. 1). We also exploited the presence of hollows – shallow, rimless, irregular depressions that often exhibit relatively high reflectance and a shallow spectral slope and are typically found inside or surrounding impact craters (Blewett et al., 2011, 2013; Thomas et al., 2014). Hollows are normally found on LRM deposits (Blewett et al., 2011, 2013); a recent survey determined that for 96% of the area covered by hollows there are local or regional associations with LRM (Thomas et al., 2014). We infer from these findings that hollows can be used at high confidence as a proxy for the presence of LRM, even when LRM cannot be directly observed from color images.

The smallest craters examined in this study lie at the transition in morphology between simple and complex craters (Pike, 1988; Barnouin et al., 2012). Therefore, two depth estimates were possible for most craters, one based on the estimated depth of excavation, and one based on the estimated source depth of central peak material. For a small number of craters, color determinations could not be made because there were inadequate color data or subsequent geological modification had obscured the color (e.g., nearby pyroclastic activity, crater ejecta, superposed craters). These craters were not used further to determine the thickness of the interior volcanic plains.

To bound the depth of origin of excavated subsurface material, we used crater scaling rules and melt volume calculations. These methods, their assumptions, and their limitations were given by Ernst et al. (2010), and we therefore describe here only the basic concepts. Material now present in the ejecta, rim, or floor of a crater was excavated during the impact event; thus, its depth of origin can by definition be no greater than the maximum depth of excavation. Material present in the central peak of a crater was uplifted coherently and without melting during excavation (Cintala and Grieve, 1998a); its minimum depth of origin is thus equal to the maximum depth of impact melting. By bounding the original location of the material exposed by these impacts, we can constrain the thickness of the volcanic surface layer and the structure of the underlying material. There are a sufficient number of well-distributed craters within Caloris to derive multiple measures of thickness across the basin.

3. Observations

From MDIS orbital images, we identified 144 craters ≥ 10 km in diameter within the Caloris interior plains (which has an area of $1.72 \times 10^6 \text{ km}^2$), of which 137 were suitable for color classification



Fig. 1. Mosaic of Caloris basin made up of MDIS images acquired during MESSENGER's orbital mission phase. The mosaic is in an orthographic projection centered on Caloris (31.5°N , 162.7°E) and is an enhanced-color composite of WAC images, in which PC2, PC1, and relative visible color (430-nm/1000-nm ratio) are shown in the red (R), green (G), and blue (B) image planes, respectively, overlain on a monochrome mosaic optimized for viewing morphology. HRP appears as brown/orange, and LRM appears as dark blue.

on the basis of the criteria defined above. The images are of sufficient resolution and appropriate viewing geometry to identify all craters greater than 10 km in diameter. Two craters less than 10 km in diameter were also included as they yield important subsurface information. These small craters are both located near the basin rim. A list of the 146 craters, along with their locations, diameters, color classifications, calculated maximum depths of excavation, and calculated minimum depths of central peak origin, is given in Table A1 in Appendix A.

3.1. Color classification

The craters were classified according to the presence or absence of LRM in their excavated and uplifted materials (ejecta, rim, floor, central peaks). Many of the observed craters excavated LRM from beneath the surface HRP layer. The locations, sizes, and color classifications of the craters within Caloris are illustrated in Fig. 2. In general, larger craters exposed LRM and smaller craters did not. The largest crater anywhere in the basin that did not expose any detectable LRM is ~30 km in diameter (34.7°N , 164.7°E). Within a radial distance of 640 km from the center of the basin, no craters smaller in diameter than 25 km exposed LRM. As seen in Fig. 2, this distance is very close to, and in some cases reaches, the rim of the basin. Two small craters (5 and 7 km in diameter) just inside the

basin rim excavated LRM, indicating a substantial thinning of the fill at the basin edge.

The craters Munch (61 km in diameter, 40.5°N , 152.9°E), Sander (52 km in diameter, 42.4°N , 154.6°E), and Poe (81 km in diameter, 43.8°N , 159.2°E) lie close to one another in the northwestern portion of the Caloris interior plains (Fig. 3). The three craters provide complex examples of the color classification approach. Munch exhibits a clear LRM signal on both its rim and its central peaks. Hollows (Blewett et al., 2011, 2013) are observed in all areas associated with LRM in this crater, although the hollows in the central peaks are subtle. Sander exhibits LRM on its walls, though to a lesser degree than Munch, and coalescing hollows cover much of the floor and central peaks. These areas of hollows are collocated with LRM.

The northeastern rim of Poe crater has been superposed by several smaller, 8- to 20-km-diameter craters (see arrow 1, Fig. 3), which have deposited HRP material on top of the LRM rim. These superposed craters reveal hollows in their rims, suggesting the presence of LRM in the shallow subsurface. Indeed, the unmodified portions of the rim exhibit a clear LRM signature, including the presence of many hollows (e.g., arrow 2, Fig. 3). The central peak of Poe is ambiguous; in the color mosaic, the peaks appear similar in color to the Caloris interior plains. At higher resolution, however, hollows can be seen (Fig. 4), similar to those on the rim and those exposed on the superposed rim craters. These hollows are likely to

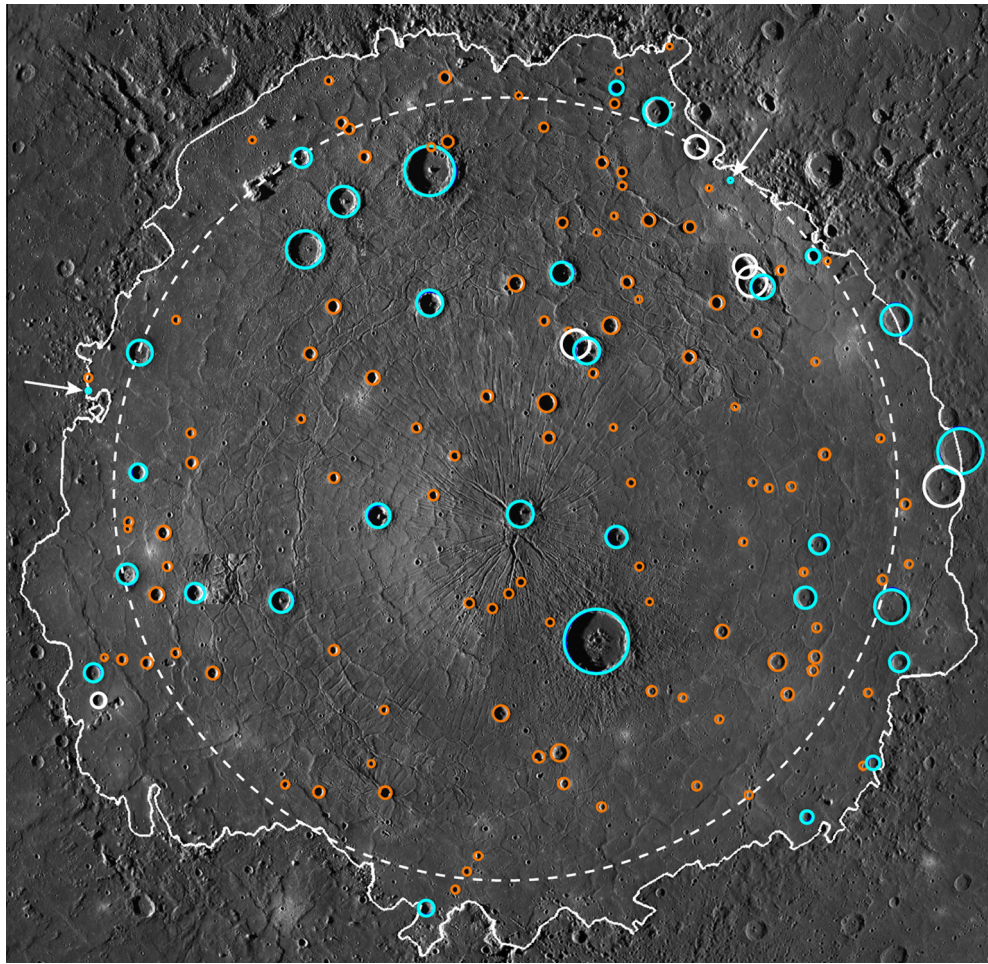


Fig. 2. Color classification of 144 craters larger than 10 km in diameter within the Caloris basin. Craters outlined in blue (30) excavated and/or uplifted spectrally distinct LRM from depth. Craters outlined in orange (107) have not exposed LRM. Craters outlined in white (7) could not be classified on the basis of color. The dashed circle indicates a distance of 640 km from the basin center. Arrows indicate the location of two small (5- and 7-km-diameter) craters near the basin rim that excavated LRM.

be similarly indicative of the presence of LRM close to the surface. Because no direct detection of LRM can be made at this location, however, Poe's central peaks will be designated here only as suggestive of LRM.

3.2. Search for flooded craters

Flooded impact craters can be used to characterize the thickness and emplacement of volcanic plains. Such relations have been demonstrated for Mercury's northern plains (Head et al., 2011), where numerous fully buried, or ghost, craters are recognizable only by the wrinkle-ridge rings formed where the buried crater rims have concentrated compressional stresses and localized contractional strain. Although no complete wrinkle ridge rings are observed in Caloris, partial ridge rings that may be suggestive of ghost craters are seen. The complex, often-polygonal pattern of contractional deformation in Caloris, however, makes a clear determination of the presence of ghost craters problematic (see also Section 4.3.3).

Orbital image analysis has revealed no partially flooded craters ≥ 10 km in diameter in the Caloris interior plains, contrary to inferences (e.g., the craters Poe, Munch, and Nawahi) from lower-resolution flyby images (Murchie et al., 2008; T.R. Watters et al., 2009b). The higher-resolution orbital images reveal that the craters previously classified as embayed actually postdate the flooding: each crater has a well-defined ejecta deposit and a secondary

crater field superposed on the surrounding interior plains. The breached appearance of Poe results from the superposition of several smaller craters on or near the northeastern portion of the rim (see arrow 1 in Fig. 3); the formation of these craters deposited HRP material on top of the LRM rim, producing the appearance of a breach at low resolution.

3.3. Thickness of the volcanic plains

The large number and widespread distribution of color-classified craters considered here, far greater than the number explored by Ernst et al. (2010), provide the means to estimate the thickness of the surface HRP as a function of position across the basin. Because of the size distribution of impactors in the inner Solar System, there are many more small craters than large craters. Of the post-plains craters inside the Caloris basin identified for this study, 32% are larger than 20 km in diameter, but only 4% are larger than 50 km in diameter. This size distribution results in a large number of measurements that provide only a lower bound on the thickness of the volcanic fill. The largest craters also complicate thickness measurements, as their formation both excavated and uplifted LRM, yielding maximum values that may be substantially larger than the actual thickness of the overlying layer. Although these large craters provide important stratigraphic information at greater depths, they do not provide accurate measures of the thickness of the surface volcanic layer. Because individual craters

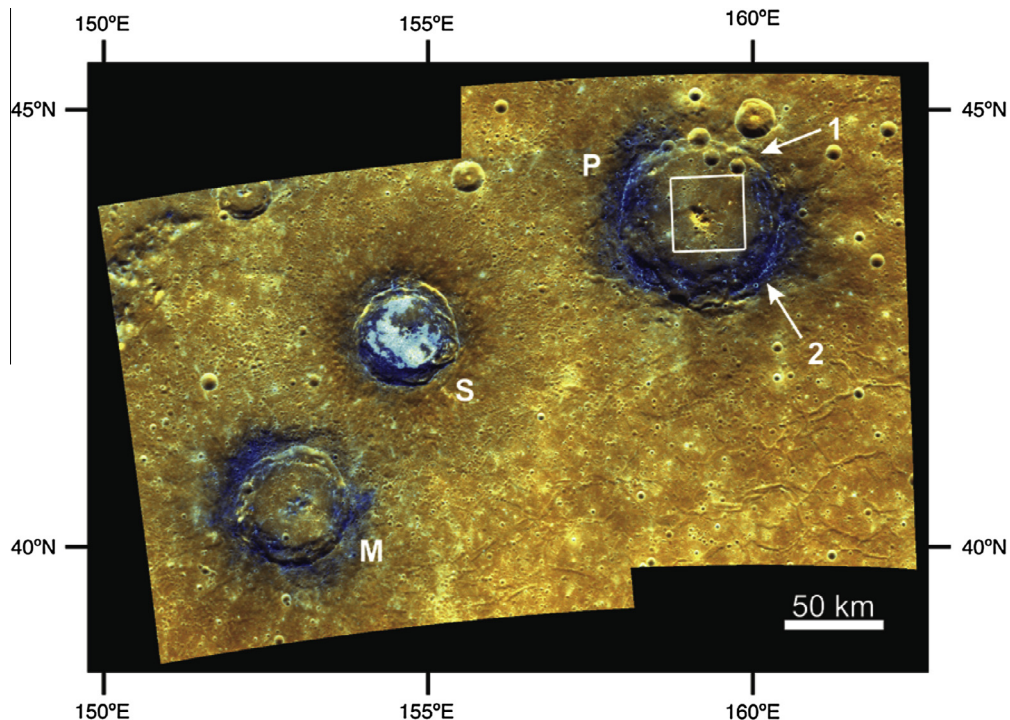


Fig. 3. Enhanced color mosaic of Munch (M), Sander (S), and Poe (P) craters. PC2, PC1, and relative color are in the R, G, and B image planes, respectively. Munch crater, 61 km in diameter, exhibits LRM and hollows on its rim and central peak. Sander crater, 52 km in diameter, exhibits LRM on its rim, floor, and central peak. The interior has been covered by coalescing hollows. Poe crater, 81 km in diameter, exhibits LRM on its rim. The northeast portion of the rim (point 1) has been covered by deposits associated with four smaller craters, masking the LRM signature of the rim in this area. These small craters exhibit hollows, indicating LRM close to the surface (point 2). The white box within Poe crater indicates the position of a targeted NAC image that is shown in Fig. 4. This mosaic is in an equirectangular projection centered at 42°N, 154°E, and was created from WAC images EW0218204194I, EW0218204190G, EW0218204186F, EW0218246495I, EW0218246491G, and EW0218246487F.

provide bounds and not absolute measures of the thickness of the surface volcanic plains, the bounds from multiple craters of varying sizes must be considered together to narrow the range of estimates for the thickness of the volcanic plains in a given region.

A plot of the depth of excavation versus radial distance from the center of Caloris (Fig. 5) allows for the characterization of the thickness of the HRP from the center to the rim of the basin. The surface layer of plains material is consistently at least ~2.5 km thick and reaches ~3.5 km thickness within a radial distance of 640 km from the basin center. These thickness values are consistent with the estimates made for the center of Caloris from MESSENGER flyby images (Ernst et al., 2010) and those inferred from fault restriction measurements in the same area (Klimczak et al., 2013). Beyond 640 km distance, LRM can appear at shallower depths. Observed (Thomson et al., 2009) and simulated (Head, 1982; Whitten and Head, 2013) thickness values for mare basalt deposits in lunar multi-ring basins also show thicker deposits in the central basin and shallower flooding within a surrounding annulus.

Applying our depth calculations only to those craters ≥ 10 km in diameter results in a lack of depth bounds shallower than 0.8 km. Smaller craters across the basin were examined, and only two, both located just inside of the Caloris rim (at 34.1°N, 143.1°E and 42.7°N, 174.9°E), excavated LRM. These simple craters, 5 and 7 km in diameter, excavated LRM from maximum depths of 0.3 and 0.5 km, respectively, revealing that the plains are substantially thinner near the rim than elsewhere in the basin.

We have assessed the degree to which the thickness of HRP material within Caloris departs from axisymmetry about the basin center. We split Caloris into northern, southern, eastern, and western quadrants (Fig. 6a). We found no systematic differences in the thickness of HRP material with azimuth (Fig. 6b). Additionally, we split the basin in half, approximately north versus south, according

to slight spectral differences noted by Murchie et al. (2008). Again, no systematic difference in the thickness of HRP was observed between the two halves.

4. Discussion

4.1. Volume and mass of Caloris interior plains

We can estimate the volume of high-reflectance plains within Caloris from the derived thickness values and the areal extent of the plains. Because of the uncertainties in our thickness estimates, we calculate conservative minimum and maximum volumes. For the minimum value, we assume that the central area within 640 km of the basin center ($\sim 1.29 \times 10^6$ km 2) is filled with plains material 2.5 km in thickness and that the exterior annulus (0.43×10^6 km 2) is of negligible thickness. Since HRP material is present in the annulus, this second assumption is conservative. For the maximum value, we assume that the central area is filled with plains material 3.5 km in thickness and that the exterior annulus is filled with plains material that is 1.5 km thick. These assumptions yield a volume estimate of $(3.2\text{--}5.2) \times 10^6$ km 3 . For an estimated density of HRP material 2700–2900 kg/m 3 , given the low-iron, basaltic composition of HRP areas (the northern plains and the Caloris interior) inferred from elemental abundance measurements by MESSENGER's X-ray Spectrometer (Nittler et al., 2011; Weider et al., 2012), this volume corresponds to a load of $\sim(9\text{--}15) \times 10^{18}$ kg on the lithosphere.

4.2. Relationship to long-wavelength deformation

As first observed in digital terrain models derived from stereo images acquired during MESSENGER's first flyby (Oberst et al.,

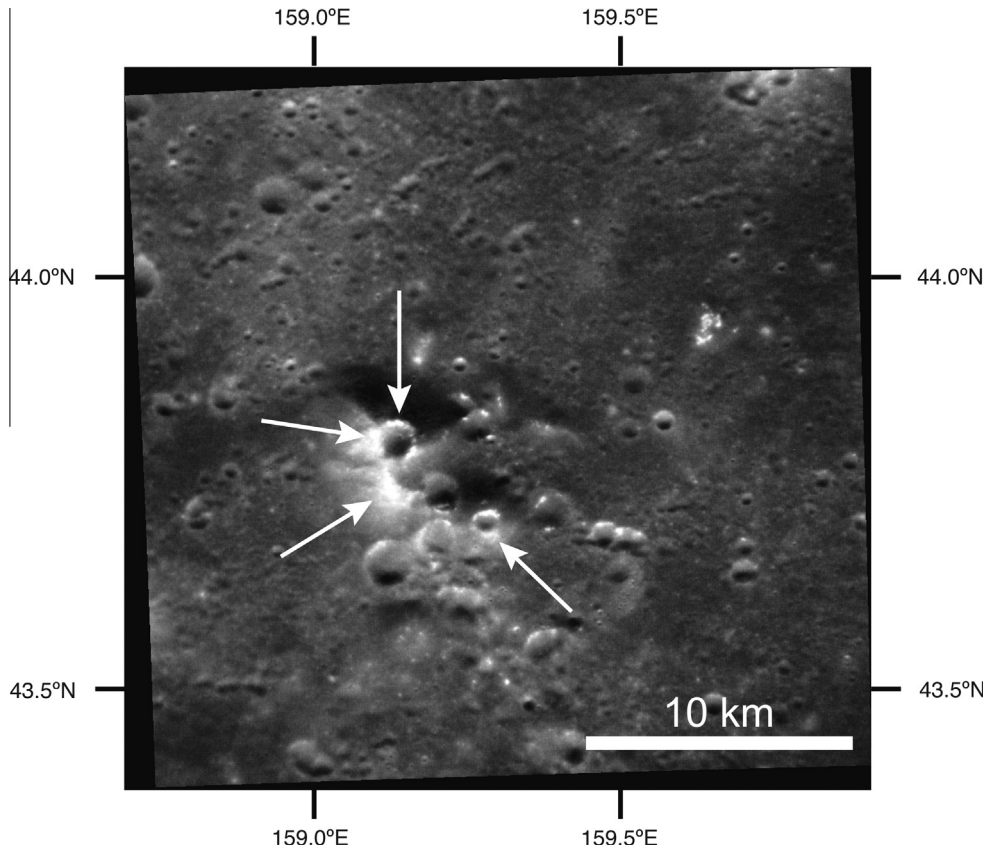


Fig. 4. Targeted NAC image (EN0218161460M) of Poe's central peak complex, corresponding to the area outlined in the white box in Fig. 3. The central peak area of Poe exhibits small hollows (white arrows), which indicate the likely presence of LRM close to the surface. The image is in an equirectangular projection centered at 43.8°N, 159.3°E.

2010) and later confirmed by Mercury Laser Altimeter (MLA) orbital measurements (Zuber et al., 2012), the interior of Caloris exhibits long-wavelength topographic undulations, including a broad rise through the northern portion of the basin. At its highest points, the elevation of the interior exceeds that of some portions of the basin rim by more than 1 km. Topographic observations in and around Caloris basin (Zuber et al., 2012) and measurements of crater tilts across the rise (Balcerski et al., 2013) indicate that much of the development of the topographic undulations occurred after the formation of the basin, the emplacement of the interior plains, and the formation of the larger post-plains craters. These measurements cannot resolve, however, whether the plains were emplaced onto an unmodified basin floor, or if some long-wavelength deformation of the basin floor predated plains volcanism.

To investigate the relationship between the Caloris interior plains and the long-wavelength topography, we distinguish broad regions of high and low elevation (Fig. 7a). Plots of excavation depth versus radial distance from the center of Caloris for craters on high- and low-elevation areas show no systematic differences in the thickness of HRP material (Fig. 7b). In other words, there is no dependence of inferred HRP thickness on long-wavelength variation in elevation within Caloris. If we assume that the surface of the lavas that formed the plains followed a gravitational equipotential surface, then the plains must have been emplaced before most, if not all, of the large-scale deformation of the basin and the surrounding area occurred.

4.3. Timing of flooding relative to basin formation

The extensive northern plains, proposed to be similar in age to the Caloris interior plains (Head et al., 2011), are host to several

hundred ghost craters (Klimczak et al., 2012; Watters et al., 2012). As mentioned in Section 3.1, we found no partially flooded or clearly defined ghost craters ≥ 10 km in diameter in the interior plains of Caloris. The absence of flooded or clearly defined ghost craters means that most of the HRP emplacement occurred within a geologically short interval, with the possible exception of thin veneers of later material; there was not sufficient time between episodes of volcanism for large craters to form and be embayed or flooded by subsequent flows.

Crater size-frequency distributions are similar for the interior and exterior plains of Caloris (Strom et al., 2008), but the density of craters at a given diameter is higher for the basin rim (Fassett et al., 2009; Denevi et al., 2013a). For the interior plains to substantially postdate the basin, there must then be a class of craters that were formed after the basin but before the emplacement of the plains that were subsequently buried by the plains material. That there is no clear evidence for the presence of such buried craters, even where the volcanic fill is thinnest within the basin, thus poses an important constraint on the timing of plains volcanism within the basin.

In addition to implying emplacement within a geologically short time interval, the absence of flooded and unambiguous ghost craters indicates that one or more of the following scenarios must hold: (1) the plains are sufficiently thick to have fully buried all craters that formed between the time of basin formation and that of plains infill; (2) most of the plains were emplaced so soon after basin formation that no large post-basin craters formed before plains infill; or (3) the complex tectonic deformation of the basin interior has rendered ghost craters unrecognizable. Here we discuss the plausibility of these three scenarios.

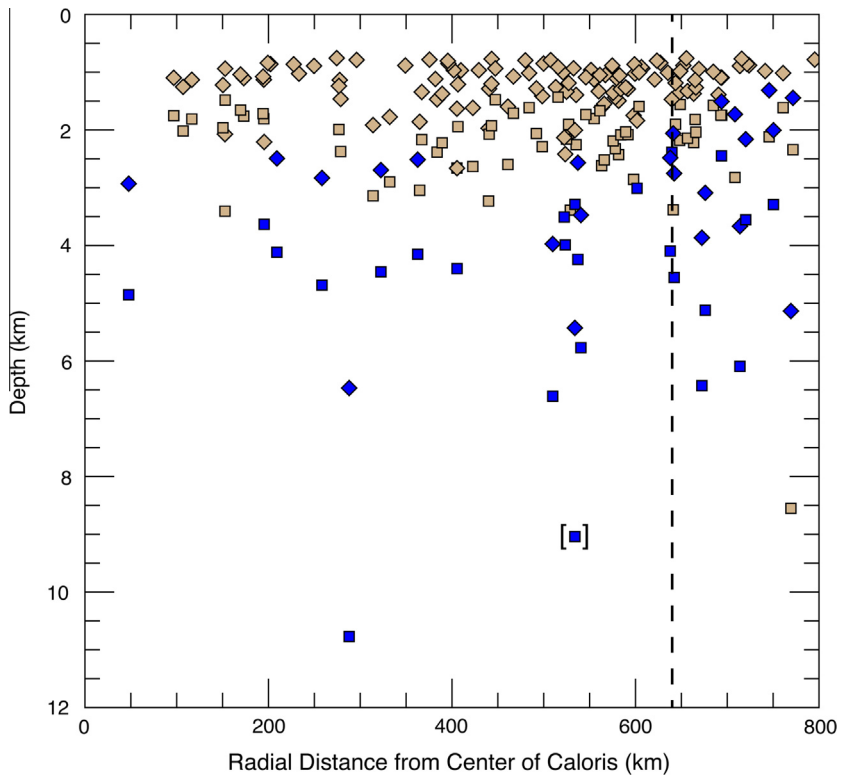


Fig. 5. Depth of excavation of crater ejecta (diamonds) and central peak material (squares) versus radial distance from the center of Caloris (31.5°N , 162.7°E) for craters ≥ 10 km in diameter. HRP is represented by tan symbols, and LRM is represented by blue symbols. The symbol representing the central peak complex of Poe is enclosed in brackets. The dashed line is at a distance of 640 km from the center of Caloris.

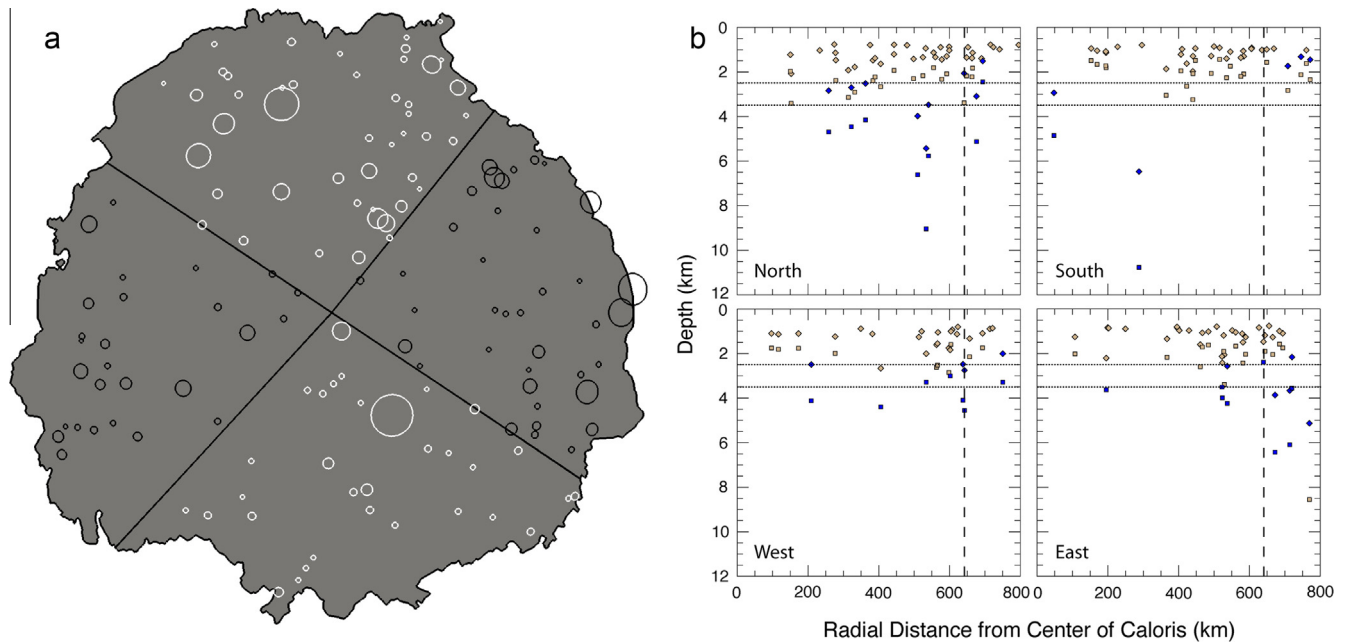


Fig. 6. (a) Division of Caloris into northern, southern, eastern, and western geographic quadrants. Circles denote craters classified by color relations. (b) Corresponding radial plots of excavation depth. Graphs show depth of excavation of crater ejecta (diamonds) and central peak material (squares) versus radial distance from the center of Caloris (31.5°N , 162.7°E) for craters ≥ 10 km in diameter in each quadrant. HRP is represented by tan symbols, and LRM is represented by blue symbols. Vertical dashed lines are at 640 km from basin center. Horizontal dotted lines denote 2.5 and 3.5 km depth below the surface.

4.3.1. Scenario 1: craters were buried by thick plains

The northern volcanic plains (NVP) host numerous ghost craters that are recognizable only by the wrinkle-ridge rings that outline their buried rims. Many craters ≥ 100 km in diameter have been

completely flooded, and several basins $\sim 200\text{--}400$ km in diameter have been nearly filled (Head et al., 2011; Klimczak et al., 2012). Larger craters closer to the center of the NVP are more likely to be completely filled, and smaller, partially filled craters are visible

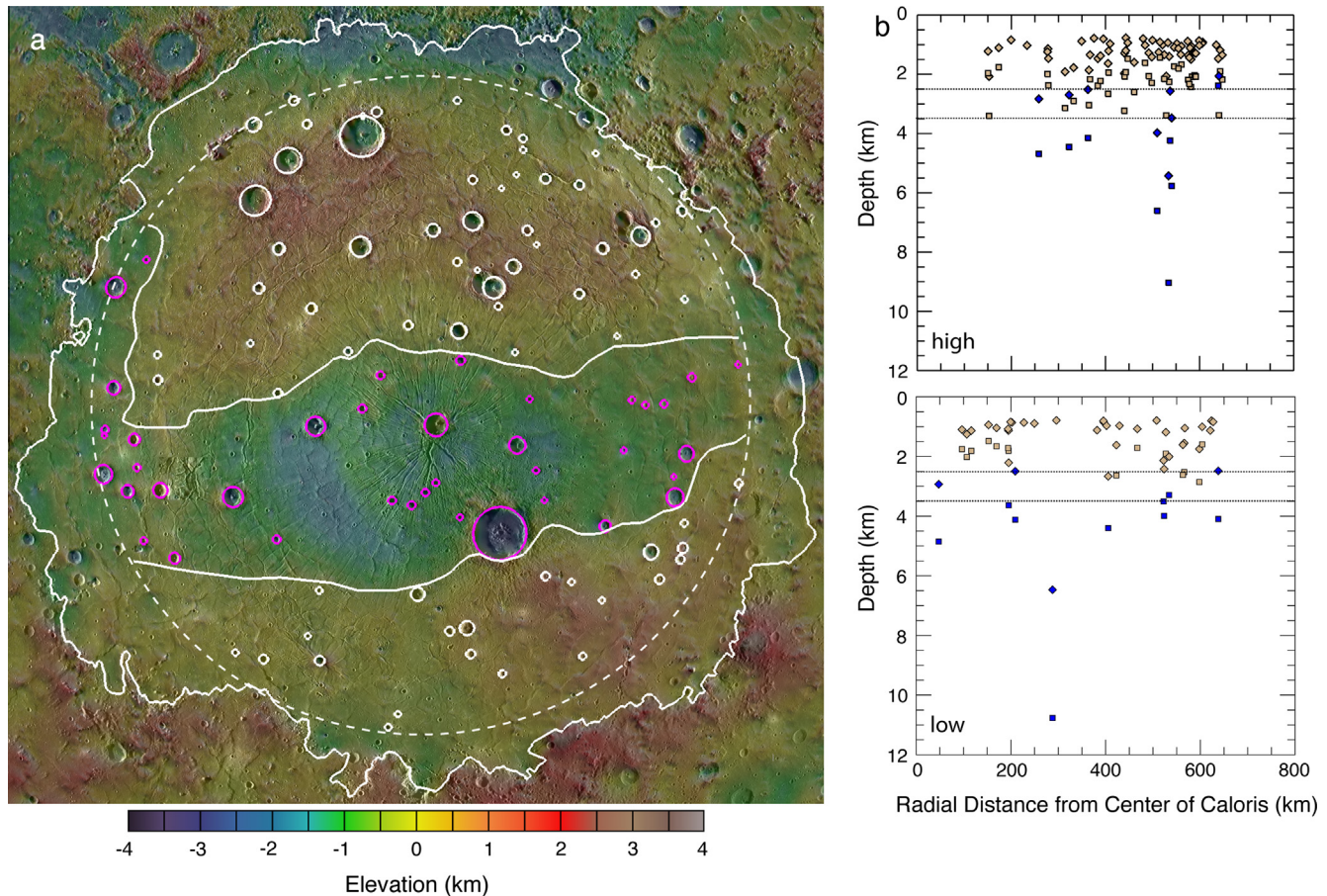


Fig. 7. Division of Caloris into areas of high and low elevation and corresponding radial plots of excavation depth. (a) Map of elevation (relative to a reference sphere with a radius of 2440 km) derived from MLA data acquired through 31 May 2014 and interpolated to 16 pixels per degree overlaid on the MDIS mosaic shown in Fig. 2. Areas of high and low elevation are separated approximately along the -0.5 km contour. (b) Depth of excavation of crater ejecta (diamonds) and central peak material (squares) versus radial distance from the center of Caloris ($31.5^\circ\text{N}, 162.7^\circ\text{E}$) for craters $\geq 10\text{ km}$ in diameter in the high- and low-elevation regions. HRP is represented by tan symbols, and LRM is represented by blue symbols. Horizontal dotted lines denote 2.5 and 3.5 km depth below the surface.

closer to the plains edges, indicating thinner plains in these regions (Klimczak et al., 2012).

Given an expanse of volcanic plains substantially larger in area than that of an individual crater, as is the case for the NVP and the Caloris interior plains, an accumulated lava thickness at least equal to a crater's rim height above the average surrounding surface is required for complete infilling and transformation into a ghost crater. MLA topographic measurements of nine relatively fresh [class 3–5, following the Trask classification criteria (see McCauley et al., 1981)] craters $100 \pm 5\text{ km}$ in diameter yield rim heights $0.8\text{--}1.3\text{ km}$ above the pre-impact surface (Susorney et al., 2013), implying that the NVP must be at least this thick to have formed the $\sim 100\text{-km}$ -diameter ghost craters that are observed. The $2.5\text{--}3.5\text{ km}$ of plains material within Caloris, therefore, would have completely filled any craters in the 100-km diameter range, but whether plains of this thickness would have erased all evidence of the flooded craters, including any wrinkle-ridge rings, is unknown. Thus, we cannot rule out the feasibility of this scenario without further modeling of crater infilling and the tectonic and topographic response to later stress fields. However, it is notable that no ghost craters of any size are observed in the outer annulus of the Caloris interior plains (which makes up $\sim 25\%$ of the total area), where the fill should be thinner, although ghost craters only partially encircled by wrinkle-ridge rings might go unnoticed because of the tectonic complexity of the region.

4.3.2. Scenario 2: flooding occurred soon after basin formation

A second scenario to consider is that the interior fill is not distinctly younger than the basin, so there was insufficient time for large craters to have formed on the post-impact basin floor. This scenario requires that the higher density of craters on the Caloris rim compared with the interior plains (Fassett et al., 2009; Denevi et al., 2013a) is not, in fact, indicative of a resolvable age difference. This possibility was also raised by Denevi et al. (2013a), as the circum-Caloris plains give conflicting indications of age. In particular, the knobby plains of the Odin Formation are morphologically and stratigraphically consistent with emplacement as Caloris basin ejecta (Murray et al., 1974; Strom et al., 1975; Trask and Guest, 1975; McCauley et al., 1981; Denevi et al., 2013a) but exhibit the lowest crater density of all the plains associated with Caloris (Denevi et al., 2013a).

Although the crater size-frequency distributions are not in doubt, the crater populations could be affected by other factors. As discussed by Denevi et al. (2013a), the higher density of craters on the rim may be the result of non-uniform self-secondary cratering (Shoemaker et al., 1968; Plescia et al., 2010; Plescia and Robinson, 2011; Hiesinger et al., 2012), the erasure of self-secondary craters by later-arriving impact melt (Zanetti et al., 2014), or differences in target material properties between ejecta deposits and impact melt (Schultz et al., 1977; Dundas et al., 2010; van der Bogert et al., 2010; Hiesinger et al., 2012), all of which have

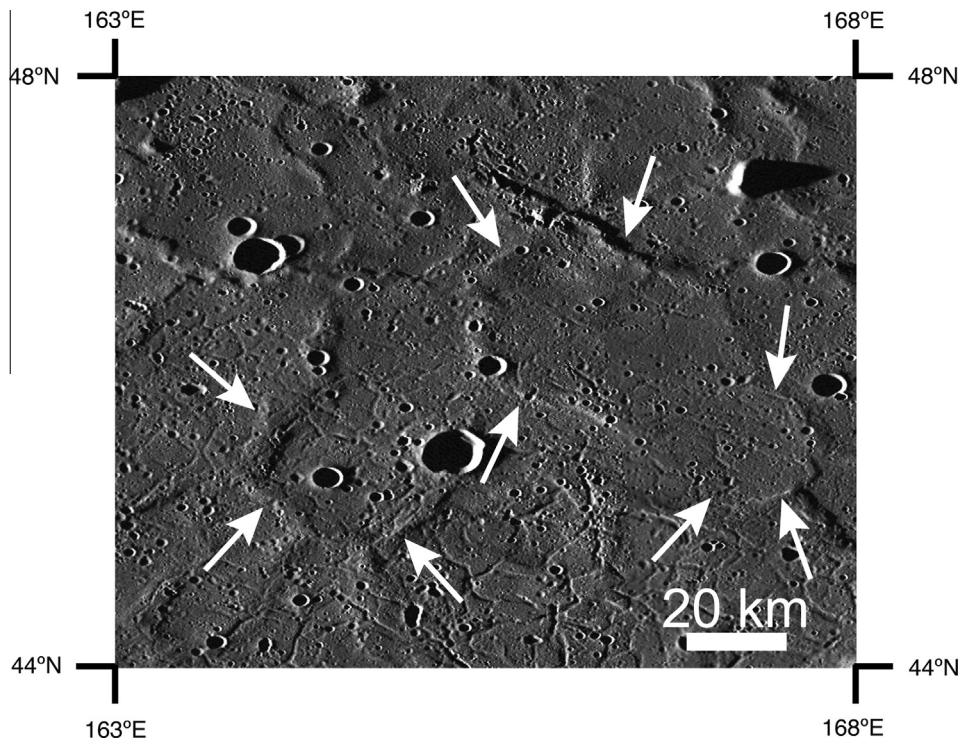


Fig. 8. Mosaic of a region in northern Caloris that displays a complex history of deformation. Arrows indicate arcuate wrinkle ridges. Graben are also evident. The mosaic is in equirectangular projection centered on 0°N, 0°E.

been shown to affect crater size–frequency distributions on the Moon.

Additionally, there are aspects inherent to the use of craters to date surfaces that may play a factor. The Caloris rim count area is made up of several smaller, disjointed areas, and the counts suffer from the statistics of small numbers at the largest sizes. The distribution of large craters across both the interior plains and the rim is uneven, with higher densities of large craters found in the northern portions of both units. Therefore, crater size–frequency distributions for smaller and larger regions of the same unit may yield different apparent crater ages. Further characterization of the crater size–frequency populations across this region may help to elucidate these issues.

4.3.3. Scenario 3: complex tectonics rendered ghost craters unrecognizable

The Caloris interior plains have been tectonically modified. The large Pantheon Fossae structure, an array of hundreds of radially oriented graben, dominates the central region of the basin, and thousands other graben of varying orientations and sizes are present throughout the interior region (Strom et al., 1975; Dzurisin, 1978; Melosh and McKinnon, 1988; Watters et al., 2005; Murchie et al., 2008; T.R. Watters et al., 2009b; Basilevsky et al., 2011; Byrne et al., 2013). Moreover, wrinkle ridges that predated the extensional structures are found across the basin (T.R. Watters et al., 2009a; Byrne et al., 2013). In addition to the troughs and wrinkle ridges, as noted above, there are long-wavelength undulations in the topography that have modified the basin interior (Oberst et al., 2010; Zuber et al., 2012). With such tectonic complexity, it is possible that ghost craters may not be distinguishable. Fig. 8 depicts an area in northern Caloris that contains complex tectonic features, including arcuate wrinkle ridges. In comparison, the northern plains do not exhibit such complex tectonics; they are dominated by wrinkle ridges, with smaller-scale graben exclusively confined to the interiors of buried craters

(Klimczak et al., 2012; Watters et al., 2012). Scenario 3, therefore, cannot be ruled out.

4.4. Caloris basin stratigraphy – what is the low-reflectance material?

Across Caloris, LRM underlies the surface HRP. Within the innermost ~640 km from the basin center, LRM has been excavated from depths as shallow as 2.5 km to as great as ~11 km (Fig. 5); no HRP material is exposed from depths greater than ~3.5 km (with the possible exception of Poe's central peaks; see Section 3.1). If these instances of LRM are sampling a single stratigraphic layer, such a layer of LRM must be at least 7.5–8.5 km thick beneath the volcanic plains throughout much of the basin.

LRM is often found in areas associated with large craters and basins, implying excavation from depth (Robinson et al., 2008; Blewett et al., 2009; Denevi et al., 2009; Ernst et al., 2010). In Caloris, the LRM may represent original basin floor material (derived from the lower crust and/or upper mantle as a product of the impact), extrusive plains material that predated the HRP, or a post-impact magmatic intrusion. Rembrandt basin (~715 km in diameter, centered at 32.8°S, 87.5°E) (T.R. Watters et al., 2009a), the second-largest well-preserved basin on Mercury, offers a clue for interpreting the nature of the Caloris LRM. Rembrandt is also flooded with volcanic HRP material (T.R. Watters et al., 2009a) that is spectrally distinct from both the basin's ejecta and portions of the basin interior that were not later flooded (Whitten et al., 2014b), both of which exhibit LRM signatures matching those excavated from beneath the Caloris volcanic plains (Fig. 9). The LRM within Rembrandt forms a hummocky unit (Whitten et al., 2014b) morphologically similar to knobby terrain on the Moon identified and mapped as directly related to basin formation (e.g., Head, 1974, 2010; McCauley, 1977). In Rembrandt, therefore, the original basin floor material can be inferred to be LRM. By analogy, the LRM exposed by craters in the Caloris interior most likely comes from the basin floor itself instead of a buried unit of volcanic

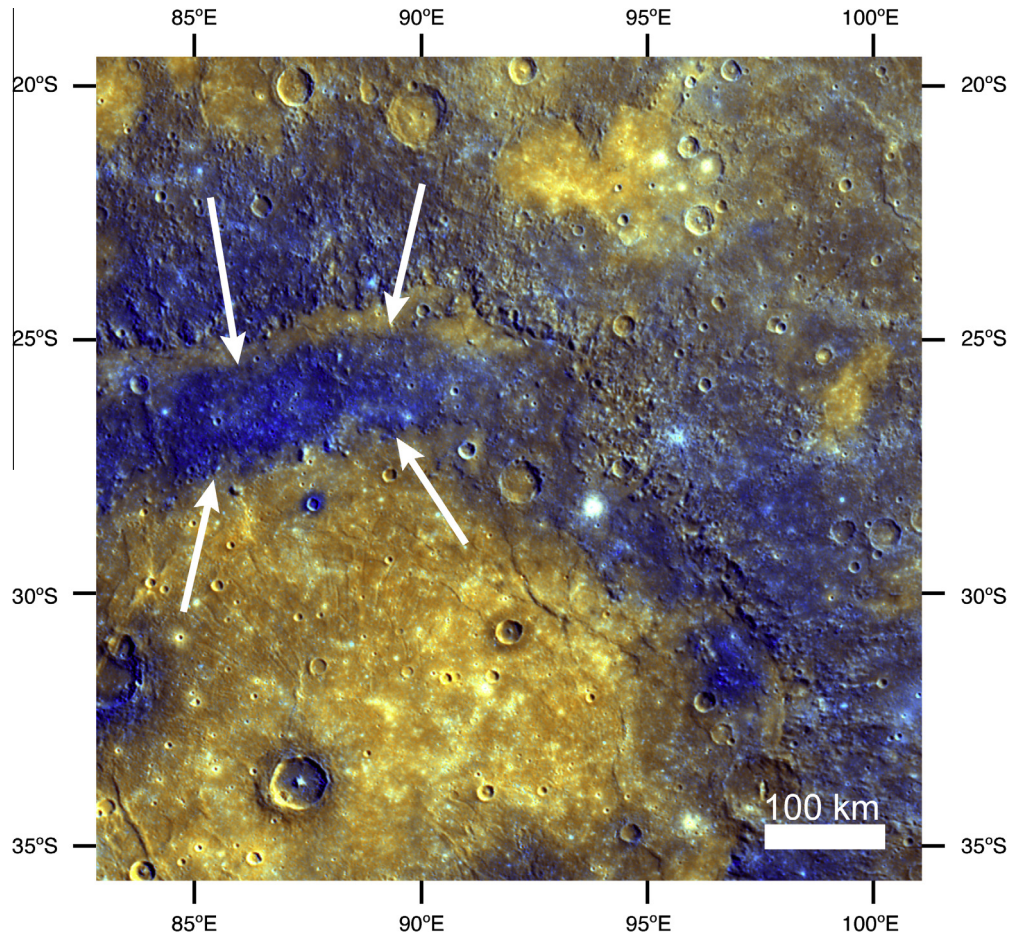


Fig. 9. A portion of the Rembrandt basin in enhanced color (PC2, PC1, 430-nm/1000-nm ratio in R, G, and B, respectively). Most of the basin interior has been flooded by younger volcanic HRP material (brown/orange) that is spectrally distinct from the basin ejecta and unfilled portions of the basin interior (dark blue, indicated by arrows), both of which exhibit LRM signatures matching those excavated from beneath the Caloris interior plains. This mosaic is in an equirectangular projection centered at 27.5°S, 92.0°E, and was created from WAC images EW0249322734I, EW0249322726G, and EW0249322730F.

or plutonic origin, although some combination of sources cannot be excluded.

4.4.1. Could the LRM be impact melt?

If the LRM excavated by the larger craters within Caloris was derived from the original basin floor, what portion of the material could be impact melt? We can calculate the volume of melt generated and retained in the basin by the Caloris-forming impact with the methods detailed by Ernst et al. (2010) and Roberts and Barnouin (2012).

The only observable quantity we have is the final size of the Caloris basin, which has been fit to an ellipse with axes of approximately 1525 by 1315 km (Fassett et al., 2009). However, the melt volume calculation also depends on the initial conditions of the impact, including the impact angle and velocity and the size of the impactor. Since our observed value is the final crater size, these three initial conditions are interrelated. With all other variables held constant, a low-velocity impact requires a larger projectile than a high-velocity impact to produce the same-sized final crater; likewise, an oblique impact requires a larger projectile than a vertical impact to produce the same final crater size (Gault and Wedekind, 1978).

For simplicity, we assume a 90° impact angle (measured with respect to the horizontal), despite the possibility that the ellipticity of the basin could signify an oblique impact. Final craters with diameters substantially smaller than the target body become

elliptical only at extremely oblique angles (<30°) (e.g., Gault and Wedekind, 1978); when the curvature of the target becomes relevant, however, elliptical basins can be produced at impact angles approaching 60° (Schultz, 1997; Cheng and Barnouin-Jha, 1999; Marinova et al., 2008). On the basis of the basin shape and the mapping of Caloris sculpture, Fassett et al. (2009) suggested that the Caloris impactor struck at a moderately oblique impact angle.

Computational (Pierazzo and Melosh, 2000; Ivanov and Artemieva, 2002) and analytical (Abramov et al., 2012) studies of the effect of impact angle on melt volume indicate volumes that are ~20% and ~38% less, respectively, for an impact angle of 45° than for a vertical impact. Because the analytical study did not include energy transferred by the horizontal velocity component, we expect that this method underestimates the volume of melt produced at a 45° impact angle; therefore, we presume that the assumption of a vertical impact will affect the calculated melt volume by ≤20%.

For a final crater ~1420 km in diameter, the geometric mean of the dimensions given by Fassett et al. (2009), the transient crater would have been ~730 km in diameter (Holsapple, 1993). Three methods were used to calculate the melt volume generated in the formation of Caloris: the analytical approach of Cintala (1992) and Cintala and Grieve (1998a,b); the computational approach of Pierazzo et al. (1997); and the analytical approach of Roberts and Barnouin (2012). All three methods were discussed by Ernst et al. (2010), who termed the Roberts and Barnouin

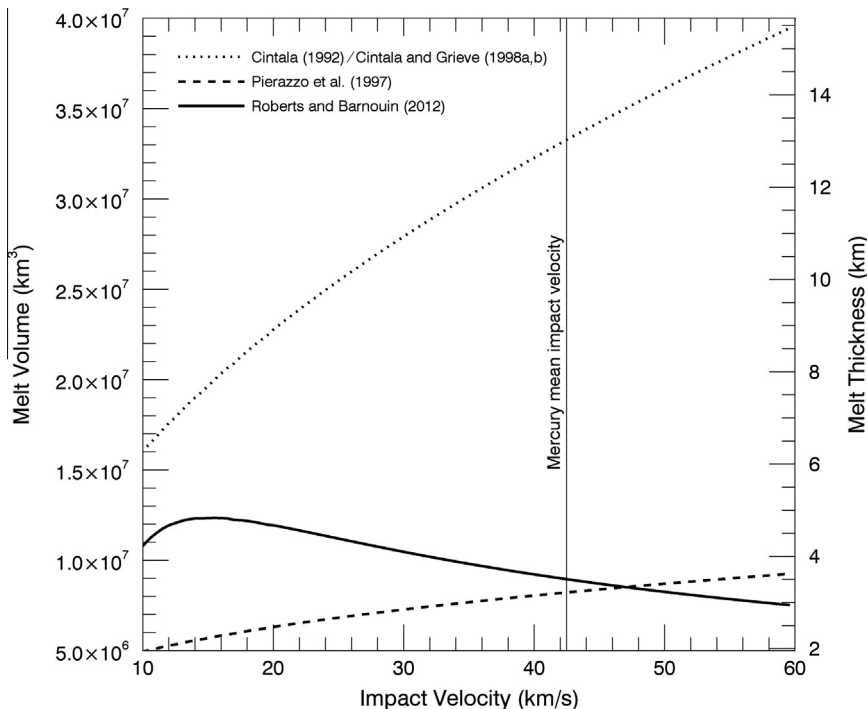


Fig. 10. Comparison of the calculated volume of impact melt and melt thickness versus impact velocity for the Caloris-forming event (for a final circular crater 1420 km in diameter) using the three methods detailed in the text: Cintala (1992) and Cintala and Grieve (1998a,b) (dotted line); Pierazzo et al. (1997) (dashed line); and Roberts and Barnouin (2012) (solid line). The melt thickness values account for the loss of melt excavated from the forming crater. The Roberts and Barnouin method includes consideration of latent heat, which accounts for the rollover at low velocities.

Table 1

Results of calculations of Caloris melt volume and melt sheet thickness.

Method ^a	Melt volume generated (km ³)			Melt sheet thickness ^b (km)		
	Min.	Max.	At 42.5 km/s	Min.	Max.	At 42.5 km/s
Cintala and Grieve	1.6×10^7	3.9×10^7	3.3×10^7	6.4	15.6	13.2
Pierazzo et al.	4.9×10^6	9.2×10^6	8.2×10^6	2.0	3.7	3.3
Roberts and Barnouin	7.5×10^6	1.2×10^7	8.9×10^6	3.0	4.9	3.5

^a From Cintala (1992) and Cintala and Grieve (1998a,b), Pierazzo et al. (1997), Roberts and Barnouin (2012).

^b Thickness calculated under the assumptions of 62% melt retention and uniform distribution across the unmodified basin (of diameter 1420 km).

method the “modified W.A. Watters et al. (2009) method.” We prefer the Roberts and Barnouin method, because it accounts for the latent heat of the melted material, which consumes a substantial amount of the impact heating and has been shown to provide the best fit to the melt seen at terrestrial craters (Ernst et al., 2010). The Cintala and Grieve and the Pierazzo et al. methods are used here for comparison. All three methods yield calculated melt volumes that are broadly consistent with the volumes observed in many terrestrial and lunar craters (Pierazzo et al., 1997; Cintala and Grieve, 1998a; Ernst et al., 2010; Abramov et al., 2012), although the Cintala and Grieve method has been shown to overestimate melt volumes for terrestrial craters (Ernst et al., 2010).

The range of total melt volume produced by a Caloris-like impact event is shown as a function of impact velocity in Fig. 10. Over the velocity range examined, the calculated volumes vary by a factor of ~2 for each method. The Roberts and Barnouin (2012) and Pierazzo et al. (1997) methods yield consistent results, remaining within a factor of ~2 of one another. The Cintala and Grieve method gives volumes that always exceed those of the other methods. The Roberts and Barnouin method yields a total melt volume generated between 7.5×10^6 and 1.2×10^7 km³. For an impact of this size, ~62% of the total melt generated would have been retained within the basin, and ~38% would have been ejected

(Cintala and Grieve, 1998a), corresponding to the retention of $(4.7\text{--}7.7) \times 10^6$ km³ of melt inside the basin. Spread uniformly across an unmodified basin (of diameter 1420 km), this melt would form a layer 3–5 km thick. For the volumes calculated by the Cintala and Grieve method, this thickness could be as large as 15 km. Minimum and maximum values for the total melt volume and thickness, as well as the values calculated using Mercury's mean impact velocity (42.5 km/s) (Le Feuvre and Wieczorek, 2008) are listed in Table 1 for all three methods.

A melt sheet of 3–15 km thickness may have differentiated during cooling (e.g., Grieve et al., 1991; Hurwitz and Kring, 2014; Vaughan and Head, 2014), but recent studies of the lunar Orientale basin have yielded conflicting results as to whether its melt sheet differentiated (Vaughan et al., 2013; Spudis et al., 2014). The composition of the Caloris LRM is currently not well determined, so any variations in composition with depth that would result from melt sheet differentiation are even more poorly constrained. Changes in composition with depth in the melt sheet might manifest themselves as variations in LRM color properties (e.g., average reflectance, spectral slope) with size of the excavating crater. No evidence for such color variations within the Caloris LRM is observed, though lack of color variation does not exclude the possibility that compositional variations with depth are present.

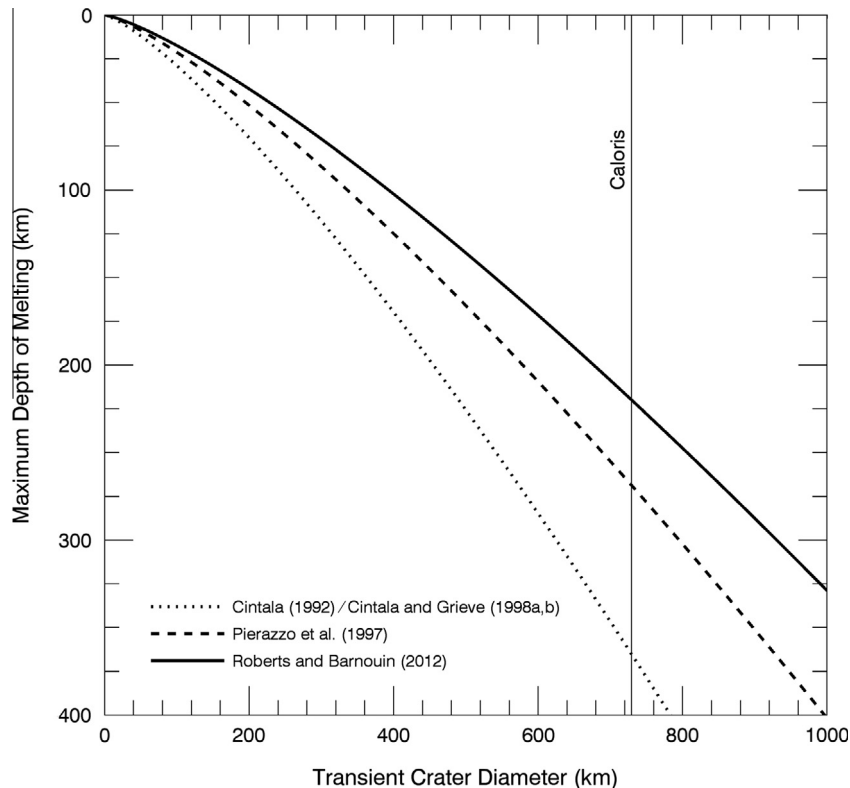


Fig. 11. Relationship between the maximum depth of melting and the transient crater diameter for Mercury, calculated with the methods of Cintala (1992) and Cintala and Grieve (1998a,b) (dotted line); Pierazzo et al. (1997) (dashed line); and Roberts and Barnouin (2012) (solid line).

Table 2

Maximum excavation and melting depths for major basins on Mercury.

Name	Rim-to-rim diameter (km)	Transient diameter (km)	Maximum depth of excavation (km)	Maximum depth of melting (km) ^a
Caloris	1420 ^b	729	73	220
Rembrandt	715	387	39	98
Tolstoj	360	206	21	44

^a From the method of Roberts and Barnouin (2012).

^b Geometric mean of major and minor axes of best-fitting ellipse (Fassett et al., 2009).

4.4.2. Source for the LRM

On the basis of our analysis, the top few kilometers of the LRM layer beneath the Caloris basin must be impact melt; it is possible that all of the excavated LRM is impact melt. LRM is also prominently associated with the Rembrandt (T.R. Watters et al., 2009a) and Tolstoj (Robinson et al., 2008) (360 km in diameter) basins. The opaque mineral phase that gives the LRM its dark and relatively blue appearance must be present in the subsurface at depths of excavation for all three of these basins. What is the source location of the LRM?

In the process of calculating melt volume, the maximum depth of melting must be determined. The relationship between the transient crater diameter and the maximum melting depth for craters on Mercury is shown in Fig. 11 using all three melt-estimation methods for vertical impacts at 42.5 km/s. As noted above, given the relationship between rim-to-rim and transient crater diameter of Holsapple (1993), a basin 1420 km in diameter corresponds to a transient cavity ~730 km in diameter. With the Roberts and Barnouin method, the Caloris impact could have melted material down to a maximum depth of 220 km beneath the surface. From the rule of thumb that the maximum excavation depth is approximately equal to one-tenth the transient crater diameter (Gault et al.,

1968; Melosh, 1989), the maximum excavation depth of the Caloris impact would have been ~73 km. The estimated transient crater diameter, maximum excavation depth, and maximum melting depth for Caloris, Rembrandt, and Tolstoj are given in Table 2.

The outer silicate shell (crust plus mantle) of Mercury is estimated to be 420 ± 30 km thick (Hauck et al., 2013). Gravity and altimetry data have been used to infer a mean crustal thickness of about 50 km (Smith et al., 2012), although this value is not well constrained and the thickness of the pre-impact crust in the Caloris area is unknown. A cross-section of Mercury's outer shell is compared with the calculated maximum depths of excavation and melting for the three basins in Fig. 12.

The Caloris impact excavated large portions of lower crustal material and possibly small amounts of upper mantle material (depending on the crustal thickness at the time of impact). Regardless of the maximum depth of excavation, the impact would have melted both lower crustal and upper mantle material. Therefore, the Caloris impact melt, and by inference the Caloris LRM, are likely to have originated as a mixture of material from the lower crust and upper mantle, with a substantial component of the latter. The excavation and melting depths during the formation of the Rembrandt basin tell a consistent story with that of Caloris: the

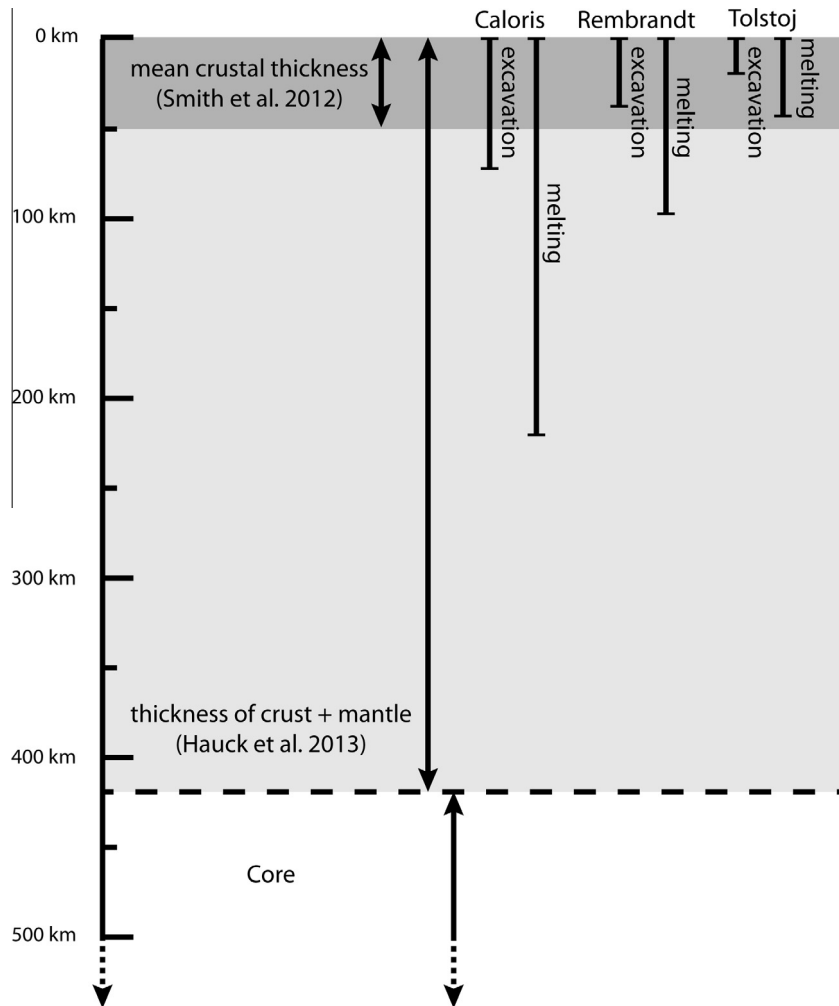


Fig. 12. Schematic cross-section of Mercury's outer silicate shell compared with the calculated maximum depths of excavation and melting for Caloris, Rembrandt, and Tolstoj basins. The Caloris impact excavated large portions of the lower crust and may have excavated material from the upper mantle. Caloris impact melt was likely derived from a combination of lower crust and upper mantle material.

impact would have excavated material from the lower crust and the melt likely originated primarily from the lower crust, possibly with a small mantle component. Both excavation and melting during the Tolstoj basin-forming impact, in contrast, were likely confined entirely to the crust. These observations suggest that the darkening agent is derived mainly from the lower crust (consistent with results of Rivera-Valentin and Barr, 2014). However, if the crust was substantially thinner at the time of basin formation or was locally thinner than average at the site of the Tolstoj basin, or if the Tolstoj impact re-exposed material from a previous impact, it is possible that the mantle could be a source of LRM more generally. The LRM within these basins, and by extension, across the planet, holds important information about the composition of Mercury's lower crust and possibly upper mantle.

5. Conclusions

From the impact craters superposed on the Caloris interior plains we have estimated the thickness of the plains material and explored the nature of the subsurface. We formed the following conclusions:

- (1) The high-reflectance plains within the Caloris basin are consistently at least 2.5 km and as much as 3.5 km thick, and the

fill thickness does not decrease resolvably with distance from the basin center except within ~100 km of the basin rim. No correlation of fill thickness with basin azimuth is observed. The interior plains have a volume of (3.2–5.2) $\times 10^6$ km³. For a density of 2700–2900 kg/m³, this volume corresponds to $\sim(9\text{--}15) \times 10^{18}$ kg of volcanic fill. Flexure of the lithosphere induced by the load from this volume likely resulted in subsidence.

- (2) There are no recognizable embayed or clearly defined ghost craters ≥ 10 km in diameter on the Caloris interior plains, implying that the major episode of plains emplacement must have occurred within a geologically short time interval. The lack of correlation between plains thickness and elevation suggests that plains emplacement predated most, if not all, of the change in long-wavelength topography.
- (3) The absence of ghost craters in the Caloris interior plains also indicates that one or more of the following scenarios must hold: the plains are sufficiently thick to have buried all evidence of craters that formed between the Caloris impact event and the emplacement of the plains; the plains were emplaced soon after basin formation; or the complex tectonic deformation of the basin interior has made it difficult to recognize ghost craters.

- (4) Low-reflectance material has been exposed by every impact that penetrated through the surface HRP. If all occurrences of LRM are derived from a single stratigraphic layer, the subsurface LRM deposit is at least 7.5–8.5 km thick. There is no constraint on the maximum thickness of the LRM deposit. On the basis of a comparison with the distribution of LRM in Rembrandt, it is likely that the top of the LRM layer beneath HRP material in Caloris was the original basin floor.
- (5) The Caloris-forming impact is estimated to have generated a layer of impact melt 3–15 km thick. Such a layer could account for the entire source of excavated LRM. This material is predicted to have been derived from a combination of the lower crust and the upper mantle. Observations of LRM in the smaller Rembrandt and Tolstoj basins suggest that the LRM darkening agent is derived mainly from the lower crust.

Acknowledgments

The MESSENGER project is supported by the NASA Discovery Program under contracts NASW-00002 to the Carnegie Institution of Washington and NAS5-97271 to The Johns Hopkins University Applied Physics Laboratory. This research has made use of the Small Body Mapping Tool of The Johns Hopkins University Applied Physics Laboratory and the Integrated Software for Imagers and Spectrometers of the U.S. Geological Survey. We thank Norman Sleep and an anonymous reviewer for their constructive reviews of an earlier version of the manuscript.

Appendix A. Impact craters on the Caloris interior plains

See Table A1.

Table A1
Craters analyzed in this study.

ID	Crater name	Diameter (km)	Central latitude ($^{\circ}$ N)	Central longitude ($^{\circ}$ E)	Was LRM excavated?	Was LRM uplifted?	Max. depth of excavation (km)	Min. depth of origin of central peak (km)
1	Atget	102.6	25.6	166.4	Yes	Yes	6.5	10.8
2	Poe	84.8	43.7	159.1	Yes	Yes	5.4	9.0
3		79.9	30.9	183.8	Yes	No	5.1	8.6
4		69.2	29.7	182.7	Undetermined	Undetermined	4.5	7.5
5	Munch	60.5	40.5	152.9	Yes	Yes	4.0	6.6
6		58.7	25.5	179.4	Yes	Yes	3.9	6.4
7		55.4	36.4	182.1	Yes	Yes	3.7	6.1
8	Sander	52.3	42.4	154.6	Yes	Yes	3.5	5.8
9		50.7	38.7	175.1	Undetermined	Undetermined	3.4	5.6
10		49.0	36.9	166.1	Undetermined	Undetermined	3.3	5.4
11		46.0	45.8	171.6	Yes	Yes	3.1	5.1
12	Apollodorus	43.4	30.5	163.3	Yes	Yes	2.9	4.9
13		41.9	36.6	166.7	Yes	Yes	2.8	4.7
14	Nawahi	40.6	35.9	145.3	Yes	Yes	2.8	4.6
15		39.7	38.5	159.2	Yes	Yes	2.7	4.5
16		39.2	27.0	153.1	No	Yes	2.7	4.4
17		38.5	44.2	173.4	Undetermined	Undetermined	2.6	4.3
18		38.4	39.3	174.9	Undetermined	Undetermined	2.6	4.3
19	Balanchine	37.6	38.4	175.6	Yes	Yes	2.6	4.2
20		36.8	39.7	165.7	Yes	Yes	2.5	4.2
21	Cunningham	36.5	30.4	157.1	Yes	Yes	2.5	4.1
22	Kertez	36.3	27.4	146.1	Yes	Yes	2.5	4.1
23		35.3	26.5	175.5	No	Yes	2.4	4.0
24		32.0	29.5	167.5	No	Yes	2.2	3.6
25		31.2	23.3	179.4	Yes	Yes	2.2	3.6
26		30.8	28.3	176.4	No	Yes	2.1	3.5
27		29.8	34.7	164.7	No	No	2.1	3.4
28		29.7	24.1	174.0	No	No	2.1	3.4
29		29.6	44.1	152.2	Yes	No	2.1	3.4
30		28.8	23.4	145.0	Yes	Yes	2.0	3.3
31		28.8	27.0	149.3	No	Yes	2.0	3.3
32		28.2	21.3	164.7	No	No	2.0	3.2
33		27.4	37.5	167.9	No	No	1.9	3.1
34		26.5	22.9	162.3	No	No	1.9	3.0
35		26.2	31.3	146.1	No	Yes	1.8	3.0
36		25.2	39.3	163.4	No	No	1.8	2.9
37		24.8	26.8	147.5	No	No	1.7	2.9
38		24.7	22.4	145.4	Undetermined	Undetermined	1.7	2.8
39		24.5	15.2	159.2	Yes	No	1.7	2.8
40		23.0	38.3	154.6	No	No	1.6	2.7
41		22.8	25.5	171.7	No	No	1.6	2.6
42		22.7	29.1	147.6	No	No	1.6	2.6
43		22.5	38.0	173.2	No	No	1.6	2.6
44		21.8	24.0	150.3	No	No	1.5	2.5
45		21.1	46.9	169.6	Yes	Yes	1.5	2.4
46		20.9	24.1	175.7	No	No	1.5	2.4
47		20.6	39.4	178.4	No	Yes	1.5	2.4
48		20.5	36.4	153.6	No	No	1.5	2.4
49		20.5	35.7	156.6	No	No	1.5	2.4
50		20.2	19.5	177.8	Yes	No	1.4	2.3
51		20.0	44.9	160.0	No	No	1.4	2.3
52		19.7	41.5	170.3	No	No	1.4	2.3

53	19.4	19.8	157.6	No	No	1.4	2.3
54	19.3	47.6	159.8	No	n/a	1.4	2.2
55	19.1	39.1	168.9	No	No	1.4	2.2
56	19.1	45.6	154.1	No	No	1.4	2.2
57	18.8	22.8	174.4	No	No	1.4	2.2
58	18.7	45.4	154.6	No	No	1.3	2.2
59	18.6	36.1	171.5	No	No	1.3	2.2
60	18.6	41.1	172.4	No	No	1.3	2.2
61	18.5	43.9	168.2	No	n/a	1.3	2.2
62	18.4	24.1	147.4	No	No	1.3	2.1
63	18.2	17.8	174.8	Yes	No	1.3	2.1
64	17.9	19.7	154.9	No	No	1.3	2.1
65	17.8	44.2	155.6	No	No	1.3	2.1
66	17.8	21.2	163.9	No	No	1.3	2.1
67	17.7	20.1	164.8	No	No	1.3	2.1
68	17.5	29.3	180.7	No	No	1.3	2.0
69	17.4	23.6	175.5	No	No	1.3	2.0
70	17.4	31.9	148.5	No	n/a	1.3	2.0
71	17.3	33.4	164.7	No	No	1.3	2.0
72	17.1	31.8	155.1	No	No	1.2	2.0
73	16.8	35.0	161.9	No	No	1.2	2.0
74	16.6	23.5	168.6	No	No	1.2	1.9
75	16.5	41.6	165.9	No	No	1.2	1.9
76	16.3	31.7	177.2	No	No	1.2	1.9
77	16.3	26.6	179.1	No	No	1.2	1.9
78	15.5	37.8	164.7	No	n/a	1.1	1.8
79	15.5	46.3	169.3	No	No	1.1	1.8
80	15.5	31.2	159.5	No	No	1.1	1.8
81	15.4	27.0	162.0	No	No	1.1	1.8
82	15.4	43.5	169.2	No	No	1.1	1.8
83	15.4	29.4	145.9	No	n/a	1.1	1.8
84	15.3	25.3	155.4	No	n/a	1.1	1.8
85	15.1	39.0	176.7	No	n/a	1.1	1.8
86	15.1	33.8	158.7	No	No	1.1	1.8
87	15.0	32.7	160.4	No	No	1.1	1.8
88	14.9	22.4	177.9	No	No	1.1	1.7
89	14.9	24.1	146.3	No	No	1.1	1.7
90	14.8	19.1	166.4	No	No	1.1	1.7
91	14.7	27.2	161.1	No	No	1.1	1.7
92	14.6	30.7	175.5	No	No	1.1	1.7
93	14.4	19.6	170.3	No	n/a	1.1	1.7
94	14.2	25.2	175.9	No	No	1.0	1.7
95	14.2	27.9	147.9	No	n/a	1.0	1.7
96	14.1	27.5	162.7	No	No	1.0	1.7
97	13.9	35.7	166.9	No	n/a	1.0	1.6
98	13.9	45.4	165.2	No	n/a	1.0	1.6
99	13.8	36.7	174.9	No	No	1.0	1.6
100	13.8	19.5	177.4	No	No	1.0	1.6
101	13.7	16.7	160.9	No	n/a	1.0	1.6
102	13.6	24.6	148.6	No	No	1.0	1.6
103	13.6	33.1	148.3	No	n/a	1.0	1.6
104	13.4	27.0	180.4	No	No	1.0	1.6
105	13.3	19.0	172.4	No	No	1.0	1.6
106	13.3	47.3	153.1	No	n/a	1.0	1.6
107	13.1	23.0	157.5	No	n/a	1.0	1.5
108	13.1	31.1	173.7	No	n/a	1.0	1.5
109	13.0	30.8	174.5	No	n/a	1.0	1.5
110	13.0	35.3	177.5	No	n/a	1.0	1.5
111	12.9	19.9	153.5	No	n/a	1.0	1.5
112	12.7	15.9	160.4	No	n/a	0.9	1.5
113	12.6	27.9	163.3	No	No	0.9	1.5
114	12.6	23.1	169.9	No	No	0.9	1.5
115	12.6	37.3	146.9	No	n/a	0.9	1.5
116	12.5	42.9	169.1	No	n/a	0.9	1.5
117	12.3	17.3	161.4	No	n/a	0.9	1.4
118	12.2	22.2	171.4	No	No	0.9	1.4
119	12.0	34.6	143.0	No	n/a	0.9	1.4
120	11.9	28.3	168.4	No	n/a	0.9	1.4
121	11.9	44.7	159.1	No	n/a	0.9	1.4
122	11.8	46.8	163.9	No	n/a	0.9	1.4
123	11.8	34.0	153.4	No	n/a	0.9	1.4
124	11.8	47.6	169.8	No	n/a	0.9	1.4
125	11.5	42.5	173.7	No	n/a	0.9	1.4
126	11.5	26.4	164.4	No	n/a	0.9	1.4
127	11.5	31.5	168.3	No	n/a	0.9	1.3
128	11.5	24.0	145.5	No	n/a	0.9	1.3
129	11.4	28.9	173.0	No	n/a	0.9	1.3
130	11.4	20.9	157.0	No	n/a	0.9	1.3

(continued on next page)

Table A1 (continued)

ID	Crater name	Diameter (km)	Central latitude (°N)	Central longitude (°E)	Was LRM excavated?	Was LRM uplifted?	Max. depth of excavation (km)	Min. depth of origin of central peak (km)
131		11.2	33.6	167.6	No	n/a	0.8	1.3
132		11.2	32.0	180.0	No	n/a	0.8	1.3
133		10.7	34.0	173.3	No	n/a	0.8	1.3
134		10.6	29.1	145.9	No	n/a	0.8	1.2
135		10.6	41.7	168.6	No	n/a	0.8	1.2
136		10.5	27.4	175.6	No	n/a	0.8	1.2
137		10.4	26.9	168.7	No	n/a	0.8	1.2
138		10.4	38.4	169.4	No	n/a	0.8	1.2
139		10.4	48.5	173.0	No	n/a	0.8	1.2
140		10.2	41.1	167.6	No	n/a	0.8	1.2
141		10.2	44.7	149.3	No	n/a	0.8	1.2
142		10.1	46.0	172.5	Undetermined	Undetermined	0.8	1.2
143		10.0	39.1	179.2	No	n/a	0.8	1.2
144		10.0	37.4	165.8	No	n/a	0.8	1.2
145		6.9	42.8	174.9	No	Yes	0.5	0.8
146		5.1	34.1	143.1	No	Yes	0.4	0.6

References

- Abramov, O., Wong, S.M., Kring, D.A., 2012. Differential melt scaling for oblique impacts on terrestrial planets. *Icarus* 218, 906–916.
- Balcerski, J.A. et al., 2013. New constraints on timing and mechanisms of regional tectonism from Mercury's tilted craters. *Lunar Planet. Sci.* 44, Abstract 2444.
- Barnouin, O.S. et al., 2012. The morphology of craters on Mercury: Results from MESSENGER flybys. *Icarus* 219, 414–427.
- Basilevsky, A.T. et al., 2011. History of tectonic deformation in the interior plains of the Caloris basin, Mercury. *Solar Syst. Res.* 45, 471–497.
- Blewett, D.T. et al., 2009. Multispectral images of Mercury from the first MESSENGER flyby: Analysis of global and regional color trends. *Earth Planet. Sci. Lett.* 285, 272–282.
- Blewett, D.T. et al., 2011. Hollows on Mercury: MESSENGER evidence for geologically recent volatile-related activity. *Science* 333, 1856–1859.
- Blewett, D.T. et al., 2013. Mercury's hollows: Constraints on formation and composition from analysis of geological setting and spectral reflectance. *J. Geophys. Res. Planets* 118, 1013–1032.
- Byrne, P.K. et al., 2013. Tectonic complexity within volcanically infilled craters and basins on Mercury. *Lunar Planet. Sci.* 44, Abstract 1261.
- Chapman, C.R. et al., 2011. Small craters (secondaries) on Mercury's northern plains. *EPSC-DPS Joint Meeting* 2011, Abstract 1497.
- Cheng, A.F., Barnouin-Jha, O.S., 1999. Giant craters on Mathilde. *Icarus* 140, 34–48.
- Cintala, M.J., 1992. Impact-induced thermal effects in the lunar and mercurian regoliths. *J. Geophys. Res.* 97, 947–973.
- Cintala, M.J., Grieve, R.A.F., 1998a. Scaling impact-melt and crater dimensions: Implications for the lunar cratering record. *Meteorit. Planet. Sci.* 33, 889–912.
- Cintala, M.J., Grieve, R.A.F., 1998b. Erratum: Scaling impact melting and crater dimensions: Implications for the lunar cratering record. *Meteorit. Planet. Sci.* 33, 1343.
- Cintala, M.J., Wood, C.A., Head, J.W., 1977. The effects of target characteristics on fresh crater morphology – Preliminary results for the Moon and Mercury. *Proc. Lunar Sci. Conf.* 8, 3409–3425.
- Denevi, B.W. et al., 2009. The evolution of Mercury's crust: A global perspective from MESSENGER. *Science* 324, 613–618.
- Denevi, B.W. et al., 2013a. The distribution and origin of smooth plains on Mercury. *J. Geophys. Res. Planets* 118, 891–907.
- Denevi, B.W. et al., 2013b. The volcanic origin of a region of intercrater plains on Mercury. *Lunar Planet. Sci.* 44, Abstract 1218.
- Dundas, C.M. et al., 2010. Role of material properties in the cratering record of young platy-ridged lava on Mars. *Geophys. Res. Lett.* 37, L12203. <http://dx.doi.org/10.1029/2010GL042869>.
- Dzurisin, D., 1978. The tectonic and volcanic history of Mercury as inferred from studies of scarps, ridges, troughs, and other lineaments. *J. Geophys. Res.* 83, 4883–4906.
- Ernst, C.M. et al., 2010. Exposure of spectrally distinct material by impact craters on Mercury: Implications for global stratigraphy. *Icarus* 209, 210–223.
- Fassett, C.I. et al., 2009. Caloris impact basin: Exterior geomorphology, stratigraphy, morphometry, radial sculpture, and smooth plains deposits. *Earth Planet. Sci. Lett.* 285, 297–308.
- Gault, D.E., Wedekind, J.A., 1978. Experimental studies of oblique impact. *Proc. Lunar Planet. Sci. Conf.* 9, 3843–3875.
- Gault, D.E., Quaide, W.L., Oberbeck, V.R., 1968. Impact cratering mechanics and structure. In: French, B.M., Short, N.M. (Eds.), *Shock Metamorphism of Natural Materials*. Mono Book Corp., Baltimore, Md., pp. 87–99.
- Grieve, R.A.F., Stöffler, D., Deutsch, A., 1991. The Sudbury structure: Controversial or misunderstood? *J. Geophys. Res.* 96, 22753–22764.
- Hauke II, S.A. et al., 2013. The curious case of Mercury's internal structure. *J. Geophys. Res. Planets* 118, 1204–1220.
- Hawkins III, S.E. et al., 2007. The Mercury Dual Imaging System on the MESSENGER spacecraft. *Space Sci. Rev.* 131, 247–338.
- Hawkins III, S.E. et al., 2009. In-flight performance of MESSENGER's Mercury Dual Imaging System. In: Hoover, R.B., Levin, G.V., Rozanov, A.Y., Retherford, K.D. (Eds.), *Instruments and Methods for Astrobiology and Planetary Missions*. SPIE Proceedings, vol. 7441, Paper 7441A-3. SPIE, Bellingham, Wash., 12pp.
- Head, J.W., 1974. Orientale multi-ringed basin interior and implications for the petrogenesis of lunar highland samples. *Moon* 11, 327–356.
- Head, J.W., 1982. Lava flooding of ancient planetary crusts – Geometry, thickness, and volumes of flooded lunar impact basins. *Moon Planets* 26, 61–88.
- Head, J.W., 2010. Transition from complex craters to multi-ringed basins on terrestrial planetary bodies: Scale-dependent role of the expanding melt cavity and progressive interaction with the displaced zone. *Geophys. Res. Lett.* 37, L02203. <http://dx.doi.org/10.1029/2009GL041790>.
- Head, J.W. et al., 2008. Volcanism on Mercury: Evidence from the first MESSENGER flyby. *Science* 321, 69–72.
- Head, J.W. et al., 2011. Flood volcanism in the northern high latitudes of Mercury revealed by MESSENGER. *Science* 333, 1853–1856.
- Hiesinger, H. et al., 2012. How old are young lunar craters? *J. Geophys. Res.* 117, E00H10. <http://dx.doi.org/10.1029/2011JE003935>.
- Holsapple, K.A., 1993. The scaling of impact processes in planetary sciences. *Annu. Rev. Earth Planet. Sci.* 21, 333–373.
- Hurwitz, D.M., Kring, D.A., 2014. Differentiation of the South Pole-Aitken basin impact melt sheet: Implications for lunar exploration. *J. Geophys. Res. Planets* 119, 1110–1133. <http://dx.doi.org/10.1002/2013JE004530>.
- Ivanov, B.A., Artemieva, N.A., 2002. Numerical modeling of the formation of large impact craters. In: Koehler, C., MacLeod, K.G. (Eds.), *Catastrophic Events and Mass Extinctions: Impacts and Beyond*. Special Paper 356. Geological Society of America, Boulder, Colo., pp. 619–630.
- Keller, M.R. et al., 2013. Time-dependent calibration of MESSENGER's wide-angle camera following a contamination event. *Lunar Planet. Sci.* 44, Abstract 1719.
- Klimczak, C. et al., 2012. Deformation associated with ghost craters and basins in volcanic smooth plains on Mercury: Strain analysis and implications for plains evolution. *J. Geophys. Res.* 117, E00L03. <http://dx.doi.org/10.1029/2012JE004100>.
- Klimczak, C. et al., 2013. Insights into the subsurface structure of the Caloris basin, Mercury, from assessments of mechanical layering and changes in long-wavelength topography. *J. Geophys. Res. Planets* 118, 2030–2044.
- Le Feuvre, M., Wieczorek, M.A., 2008. Nonuniform cratering of the terrestrial planets. *Icarus* 197, 291–306.
- Malin, M.C., 1976. Observations of intercrater plains on Mercury. *Geophys. Res. Lett.* 3, 581–584.
- Marchi, S. et al., 2013. Global resurfacing of Mercury 4.0–4.1 billion years ago by heavy bombardment and volcanism. *Nature* 499, 59–61.
- Marinova, M.M., Aharonson, O., Asphaug, E., 2008. Mega-impact formation of the Mars hemispheric dichotomy. *Nature* 453, 1216–1219.
- McCauley, J.F., 1977. Orientale and Caloris. *Phys. Earth Planet. Inter.* 15, 220–250.
- McCauley, J.F. et al., 1981. Stratigraphy of the Caloris basin, Mercury. *Icarus* 47, 184–202.
- Melosh, H.J., 1989. Impact Cratering: A Geologic Process. Oxford University Press, New York, 245pp.
- Melosh, H.J., McKinnon, W.B., 1988. The tectonics of Mercury. In: Vilas, F., Chapman, C.R., Matthews, M.S. (Eds.), *Mercury*. University of Arizona Press, Tucson, pp. 374–400.
- Murchie, S.L. et al., 2008. Geology of the Caloris basin, Mercury: A view from MESSENGER. *Science* 321, 73–76.
- Murray, B.C. et al., 1974. Mercury's surface: Preliminary description and interpretation from Mariner 10 pictures. *Science* 185, 169–179.
- Murray, B.C. et al., 1975. Surface history of Mercury – Implications for terrestrial planets. *J. Geophys. Res.* 80, 2508–2514.
- Nittler, L.R. et al., 2011. The major-element composition of Mercury's surface from MESSENGER X-ray spectrometry. *Science* 333, 1847–1850.

- Oberst, J. et al., 2010. The morphology of Mercury's Caloris basin as seen in MESSENGER stereo topographic models. *Icarus* 209, 230–238.
- Pierazzo, E., Melosh, H.J., 2000. Melt production in oblique impacts. *Icarus* 145, 252–261.
- Pierazzo, E., Vickery, A.M., Melosh, H.J., 1997. A reevaluation of impact melt production. *Icarus* 127, 408–423.
- Pike, R.J., 1988. Geomorphology of impact craters on Mercury. In: Vilas, F., Chapman, C.R., Matthews, M.S. (Eds.), *Mercury*. University of Arizona Press, Tucson, Ariz, pp. 165–273.
- Plescia, J.B., Robinson, M.S., 2011. New constraints on the absolute lunar cratering chronology. *Lunar Planet. Sci.* 42, Abstract 1839.
- Plescia, J.B., Robinson, M.S., Paige, D.A., 2010. Giordano Bruno: The young and the restless. *Lunar. Planet. Sci.* 41, Abstract 2038.
- Rivera-Valentin, E.G., Barr, A.C., 2014. Impact-induced compositional variations on Mercury. *Earth Planet. Sci. Lett.* 391, 234–242.
- Roberts, J.H., Barnouin, O.S., 2012. The effect of the Caloris impact on the mantle dynamics and volcanism of Mercury. *J. Geophys. Res.* 117, E02007. <http://dx.doi.org/10.1029/2011JE003876>.
- Robinson, M.S. et al., 2008. Reflectance and color variations on Mercury: Regolith processes and compositional heterogeneity. *Science* 321, 66–69.
- Schultz, P.H., 1997. Forming the South-pole Aitken basin – The extreme games. *Lunar Planet. Sci.* 28, Abstract 1259.
- Schultz, P.H., Gault, D., Greeley, R., 1977. Interpreting statistics of small lunar craters. *Proc. Lunar Sci. Conf.* 8, 3539–3564.
- Shoemaker, E.M. et al., 1968. Television observations from Surveyor VII. In: Surveyor VII Mission Report, Part 2. NASA Technical Report. Pasadena, Calif, pp. 75–134.
- Smith, D.E. et al., 2012. Gravity field and internal structure of Mercury from MESSENGER. *Science* 336, 214–217.
- Spudis, P.D., Martin, D.J.P., Kramer, G., 2014. Geology and composition of the Orientale basin impact melt sheet. *J. Geophys. Res. Planets* 119, 19–29.
- Strom, R.G., 1977. Origin and relative age of lunar and mercurian intercrater plains. *Phys. Earth Planet. Inter.* 15, 156–172.
- Strom, R.G. et al., 1975. Preliminary imaging results from the second Mercury encounter. *J. Geophys. Res.* 80, 2345–2356.
- Strom, R.G. et al., 2008. Mercury cratering record viewed from MESSENGER's first flyby. *Science* 321, 79–81.
- Susorney, H.C. et al., 2013. Impact crater morphology on Mercury from MESSENGER observations. *Lunar Planet. Sci.* 44, Abstract 1650.
- Thomas, R.J. et al., 2014. Hollows on Mercury: Materials and mechanisms involved in their formation. *Icarus* 229, 221–235.
- Thomson, B.J. et al., 2009. A new technique for estimating the thickness of mare basalts in Imbrium basin. *Geophys. Res. Lett.* 36, L12201. <http://dx.doi.org/10.1029/2009GL037600>.
- Trask, N.J., Guest, J.E., 1975. Preliminary geologic terrain map of Mercury. *J. Geophys. Res.* 80, 2461–2477.
- van der Bogert, C.H. et al., 2010. Discrepancies between crater size-frequency distributions on ejecta and impact melt pools at lunar craters: An effect of differing target properties? *Lunar Planet. Sci.* 41, Abstract 2165.
- Vaughan, W.M., Head, J.W., 2014. Impact melt differentiation in the South Pole-Aitken basin: Some observations and speculations. *Planet. Space Sci.* 91, 101–106.
- Vaughan, W.M. et al., 2013. Geology and petrology of enormous volumes of impact melt on the Moon: A case study of the Orientale basin impact melt sea. *Icarus* 223, 749–765.
- Watters, T.R., Nimmo, F., Robinson, M.S., 2005. Extensional troughs in the Caloris basin of Mercury: Evidence of lateral crustal flow. *Geology* 33, 669–672.
- Watters, W.A., Zuber, M.T., Hager, B.H., 2009. Thermal perturbations caused by large impacts and consequences for mantle convection. *J. Geophys. Res.* 114, E02001. <http://dx.doi.org/10.1029/2007JE002964>.
- Watters, T.R. et al., 2009a. Evolution of the Rembrandt impact basin on Mercury. *Science* 324, 618–621.
- Watters, T.R. et al., 2009b. Emplacement and tectonic deformation of smooth plains in the Caloris basin, Mercury. *Earth Planet. Sci. Lett.* 285, 309–319.
- Watters, T.R. et al., 2012. Extension and contraction within volcanically buried impact craters and basins on Mercury. *Geology* 40, 1123–1126.
- Weider, S.Z. et al., 2012. Chemical heterogeneity on Mercury's surface revealed by the MESSENGER X-Ray Spectrometer. *J. Geophys. Res.* 117, E00L05. <http://dx.doi.org/10.1029/2012JE004153>.
- Whitten, J.L., Head, J.W., 2013. Detecting volcanic resurfacing of heavily cratered terrain: Flooding simulations on the Moon using Lunar Orbiter Laser Altimeter (LOLA) data. *Planet. Space Sci.* 85, 24–37.
- Whitten, J.L. et al., 2014a. Intercrater plains on Mercury: Insights into unit definition, characterization, and origin from MESSENGER data. *Icarus* 241, 97–113.
- Whitten et al., 2014b. Rembrandt basin: Distinguishing between volcanic and impact smooth plains deposits on Mercury. *Lunar Planet. Sci.* 45, Abstract 1289.
- Zanetti, M. et al., 2014. Mapping crater density variation on Copernican ejecta blankets: Evidence for auto-secondary cratering at Tycho and Aristarchus. *Lunar Planet. Sci.* 45, Abstract 1528.
- Zuber, M.T. et al., 2012. Topography of the northern hemisphere of Mercury from MESSENGER laser altimetry. *Science* 336, 217–220.